Modelling an articulated raft wave energy converter

I.F. Noad[1] and R. Porter

School of Mathematics, University Walk, Bristol, BS8 1TW, UK

Abstract

In this paper we develop an efficient mathematical solution method for an articulated raft wave energy converter. Representative of Pelamis and the Cockerell raft design, it is comprised of a series of floating pontoons connected via hinges. Power is generated through the relative motions of adjacent elements which are excited by the incident wave as it passes along the length of the device. Using an efficient semi-analytic solution we are able to generate results more quickly than would be possible using a panel-based numerical code such as WAMIT. This allows us to explore the parameter space quickly and thus to develop an understanding as to what elements of raft-type wave energy converter design allow it to generate power so successfully. We find that the capture factor increases proportionately to the number of pontoons, a focusing effect that allows the device to absorb far more power than that which is directly incident upon its frontage. Hinge position and device proportions are also significant with results favouring long, narrow rafts made up of pontoons of increasing length from fore to aft.
Keywords: hydrodynamic, wave energy converter, articulated raft, optimisation, mathematical model.

1. Introduction

Ocean waves have long been of interest as an abundant source of energy and a wide variety of devices has been conceived over the years with the intention of harnessing their potential. Indeed, in response to the oil shortage of the 1970's the UK government initiated a major Wave Energy programme. This attracted the attention of a wide range of scientists and engineers and many ideas for capturing wave energy were proposed. Of particular note is the seminal work of Stephen Salter [15], published in *Nature* in the mid 1970's it demonstrates that efficiencies up to 80% may be achieved by a cam-shaped cylindrical device called the Salter 'duck'. This was one of the earliest wave energy designs to gain funding from the programme along with the Bristol cylinder of Evans [3], the NEL oscillating water column [6] and the Cockerell raft of Sir Christopher Cockerell [2].

In general, wave energy device concepts fall into three main categories: terminators, attenuators and point absorbers. Terminators are oriented perpendicular to the incident wave direction to provide the maximum wave frontage of the device. Meanwhile, attenuators extend parallel to the incident wave direction with the intention of progressively extracting energy along the length of the device and point absorbers are small relative to the incident wavelength, generally being deployed in large arrays. All are designed with the intention of converting the oscillatory motion of sea waves into a usable form of renewable energy. An assessment of the performance of various wave energy device types can be found in [14], for example.

Early work was predominantly focused on terminator type devices, perhaps in part due to the extensive use of two-dimensional wave tank testing in which a device filled the entire width of the tank. Salter's 'duck', the Bristol Cylinder and the NEL are all terminator type devices and whilst Cockerell's raft was originally conceived as a longer attenuator type raft chain, early experiments were disappointing and the design quickly evolved into a terminator

[1]Corresponding author. Tel.:+44 7892 829 177.
Email addresses: imogen.noad@bristol.ac.uk (I.F. Noad), richard.porter@bristol.ac.uk (R. Porter).

type device too. With a single hinge and a wide frontage, this modified design was shown both theoretically and in wave tank testing to be capable of efficiencies comparable to Salter's 'duck'. However, terminators are not the only successful wave energy devices and more recently attenuator type wave energy converter design has been advocated in the development of the Pelamis, an articulated raft-type device of Ocean Power Delivery [19]. This used many of the early findings of the Cockerell raft as a starting point. Returning to an attenuator-type design by employing a longer, narrower planform than the original it consists of five articulated sections. Although having now ceased to operate, Pelamis attracted substantial investment with promising results seen in numerical modelling and tank testing leading to its full-scale deployment. Indeed, bought by E-ON UK in 2009, it was the first wave power machine to be purchased by a utility company.

Work based around the modelling of articulated raft-type devices has been largely driven by particular device concepts. The contributions of Haren, Mei and Newman, inspired by the Cockerell raft, are of particular note. In [4] Haren and Mei analyse the performance of a two-dimensional raft numerically using shallow water theory. They found that a raft made up of 'two or three' pontoons is sufficient and additional pontoons don't significantly contribute to performance. This is a feature of the two-dimensional theory and is due to the attenuation of the wave along the device's length, little energy being available to the aft pontoons in a two-dimensional setting. Newman and Mei [5] found that for optimal operation of an attenuator as much power must be absorbed by the aft section as by the fore, something which we see is not possible for a long chain of rafts in a two-dimensional setting. Meanwhile, in Newman's work [7] a slender-body theory was employed to produce theoretical upper bounds on the power which may be absorbed by a small system of pontoons. It was found there that for a system of three pontoons, both fore and aft hinges contribute equally to power absorption, the focusing effect of the raft supplying wave power to the aft of the device from beyond the wave frontage of the device. However, this is only investigated for a small raft made up of three pontoons. More recently, much of the development work associated with the Pelamis device has been carried out using numerical CFD and experimental wave tank testing.

In this paper we have set out to develop a better understanding as to what elements of raft-type wave energy converter design allow it to generate power so successfully. In particular, a number of questions remain unanswered: Is an articulated raft wave energy converter better suited to an attenuator-type design or terminator? What are the optimal device dimensions and how many pontoons are needed? Does the wave focusing effect found for a small, slender system apply for a larger number of hinges? Rather than concentrating on a particular device concept, such as the slender aspect ratio of the Pelamis or the wider planform of the Cockerell raft, a more general model will be considered. This allows a larger parameter space of applicability when considering the factors which play a role in device performance. Another interesting factor is the role played by the positioning of the hinges along the length of the device. It was suggested to be important in [4] for a two-dimensional device, asymmetry being beneficial to the performance, whilst in [7] the optimum power absorbed by a system of three pontoons was found to be insensitive to variations in the hinge positions when analysed using a slender-body theory and equal spacings were favoured in this work. So, what effect do the hinge positions have and how dependent on device proportions are they?

Numerical solvers such as WAMIT [18] could be used to answer such questions. However, we take advantage of the configuration of the raft and, by assuming a shallow draught, can apply analytic methods to the problem which leads to efficient computations. This allows us to explore parameter space quickly to the extent that we have embedded the solution of the three-dimensional problem within an optimisation scheme. Thus, in this paper we are concerned with a three-dimensional model for an articulated raft-type wave energy converter comprised of a series of buoyant, rectangular pontoons hinged together about a series of horizontal axes and situated in deep water. The pontoons oscillate as the incident wave propagates along the length of the raft and power take-off mechanisms are applied in the hinges, designed to resist the relative motions of adjacent pontoons.

In developing a mathematical solution we adopt a linearised hydrodynamic theory and exploit it to decompose the problem for a system of N pontoons into $N+2$ component parts. The complete wave structure interaction is thus described by a scattering problem associated

with the scattering of waves by a rigid plate along with $N+1$ additional problems associated the radiation of waves due to forced oscillatory motion in a set of generalised modes. We take advantage of the recent work of Porter [13] for the efficient solution to problems involving rigid plates lying on the surface of the water and extend it here. It is shown how an application of Fourier transforms in the plane of the free surface leads to $N+2$ integral equations in terms of unknown functions relating to the hydrodynamic pressure forces exerted on the underside of the raft. Application of a Galerkin expansion method with a prudent choice of basis functions then reduces each integral equation to a low-order system of linear equations the solutions of which may generally be efficiently and accurately computed. However, there are some cases in which the solution becomes numerically intense. In the case of large aspect ratios, when the raft becomes either particularly wide or particularly long, more terms are required in the Galerkin expansions increasing the numerical expense. The number of pontoons is also a factor in computation time since the number of integral equations increases with N. These cases will be considered in another paper [10], where approximations will be developed from the full theory presented here, leading to greatly simplified computations.

Theoretical results for the optimisation of power from a single device are well-known [17] and using these early results optimum power take-off may be readily identified for a system of two symmetrical pontoons. However, for larger systems with multiple points for power take-off then little analytic progress has been made. In [8] the maximum power take-off is determined for a symmetric configuration of three pontoons in antisymmetric and symmetric modes of motion. However, since the optimal tuning required in each of these modes is distinct their superposition provides a theoretical upper bound rather than an achievable optimum for the full device motion. Meanwhile, in [11] analytic results determining bounds on the optimal tuning of power take-off were derived for an array of two symmetric flap-type devices. Here, through a judicious choice of generalised modes we may extend those results to produce tight analytic bounds on optimal mechanical damping for practical power take-off systems in a symmetric configuration of three pontoons.

In section 2 of the paper we outline the hydrodynamic problems associated with the scattering and radiation of waves by the articulated raft model. We then go on to develop a description of the device motions in section 3. The use of generalised modes of motion is discussed broadly along with various sensible choices which may be made to suit our purposes. Section 4 deals with expressions for power absorption. A general expression for power take-off is derived and two special cases in which further analytic progress may be made are set out in more detail. The method of Porter [13] is then extended in section 5 to derive integral equations associated with the radiating modes, approximate solutions of which are then presented in section 6. Key elements of the numerical calculations are discussed in section 7 with results being presented in section 8. A variety of factors are considered, from the overall device proportions to the hinge positions and the number of pontoons of which the raft is comprised. Finally, in section 9 conclusions are drawn and suggestions for future work are given.

2. Formulation

We use Cartesian coordinates with the origin located in the mean free surface level and the fluid extending into $z<0$. The fluid has density ρ and is of infinite depth, inviscid and incompressible. Fluid motions are irrotational and of small amplitude. A hinged raft of thickness h and density $\rho_s<\rho$ floats on the surface of the water with shallow draught $d=\rho_s h/\rho$. It is made up of a series of N rectangular sections as shown in Figure 1, each of width $2b$ and hinged along $x=X_n$ for $n=1,...,N-1$, $-b<y<b$. This definition is extended to the fore and aft end-points which are located at $x=X_0, X_N$ so that the planform of the nth pontoon is given by

$$\mathcal{D}_n=\{(x,y)|X_{n-1}<x<X_n, -b<y<b\} \tag{2.1}$$

and its length by $a_n=X_n-X_{n-1}$. Choosing to centre the raft at the origin and to denote its overall length by $2a$ we may identify $X_0=-a$ and $X_N=a$. The horizontal plane occupied by

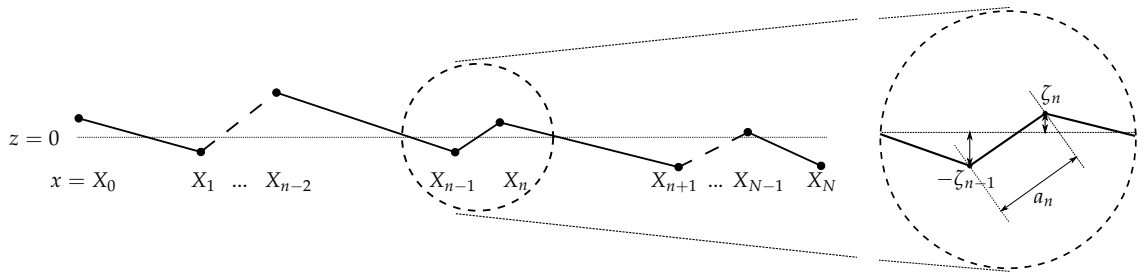

Figure 1: Some key parameters imposed on a side view (and close-up) of the articulated raft converter used in the hydrodynamic model.

the entire raft is then

$$\mathcal{D} = \bigcup_{n=1}^{N} \mathcal{D}_n = \{(x,y)| -a < x < a, -b < y < b\}. \tag{2.2}$$

Damping devices placed along each hinge enable power take-off, exerting a force opposing and in proportion to the rate of change of angle made between adjacent plates, $\dot{\Theta}_n(t)$ for $n = 1, ..., N-1$.

We assume time-harmonic incident waves of small steepness and angular frequency ω, making an angle θ with respect to the positive x-direction. The governing equation to be satisfied by the velocity potential $\Phi(x,y,z,t)$ is then

$$\nabla^2\Phi = 0, \qquad \text{for } z < 0 \tag{2.3}$$

with the combined linearised dynamic and kinematic free surface condition

$$\Phi_z + \frac{1}{g}\Phi_{tt} = 0, \qquad \text{on } z = 0 \text{ for } (x,y) \notin \mathcal{D} \tag{2.4}$$

where g is the gravitational acceleration. Meanwhile, the kinematic condition on the raft itself is

$$\Phi_z(x,y,0,t) = \frac{(x - X_{n-1})\dot{\zeta}_n(t) + (X_n - x)\dot{\zeta}_{n-1}(t)}{X_n - X_{n-1}} \qquad \text{for } (x,y) \in \mathcal{D}_n,\ n = 1, ..., N \tag{2.5}$$

where $\zeta_n(t)$ is the vertical displacement of the node at $x = X_n$ for $n = 0, ..., N$ and dots denote time derivatives. Finally, there is decay in the velocity far from the surface,

$$|\nabla\Phi| \to 0 \qquad \text{as } z \to -\infty, \tag{2.6}$$

and diffracted and radiated waves are outgoing in the far field.

The assumptions resulting in the linearised equations above allow us to both factor out harmonic time-dependence, working instead in the frequency domain, and to decompose the velocity potential into two component parts. Thus, we write

$$\Phi(x,y,z,t) = \Re\left\{\left(\frac{-iAg}{\omega}\phi^S(x,y,z) + \phi^R(x,y,z)\right)e^{-i\omega t}\right\} \quad \text{and} \quad \dot{\zeta}_n(t) = \Re\left\{\eta_n e^{-i\omega t}\right\} \tag{2.7}$$

where A is the amplitude of the incident wave, $\phi^S(x,y,z)$ represents the scattering of the incident wave by a fixed horizontal raft and $\phi^R(x,y,z)$ represents the radiation of waves due to the forced oscillatory motion of the raft. Using (2.7) in (2.3), (2.4) and (2.6) we find that ϕ^S and ϕ^R

satisfy

$$\nabla^2 \phi^{S,R}(x,y,z) = 0 \qquad \text{on } z < 0 \tag{2.8}$$

along with decay in the velocity far from the surface

$$|\nabla \phi^{S,R}| \to 0 \qquad \text{as } z \to -\infty \tag{2.9}$$

and the combined kinematic and dynamic free surface condition

$$\phi_z^{S,R}(x,y,0) = K\phi^{S,R}(x,y,0) \qquad \text{for } (x,y) \notin \mathcal{D} \tag{2.10}$$

where, $K = \omega^2/g$ is the wavenumber. Further, from (2.5) the kinematic condition on the fixed raft associated with the scattering problem is

$$\frac{\partial \phi^S}{\partial z}(x,y,0) = 0 \qquad \text{for } (x,y) \in \mathcal{D}, \tag{2.11}$$

whilst the forced motions of the radiation problem are described by

$$\frac{\partial \phi^R}{\partial z}(x,y,0) = \frac{(x - X_{n-1})\eta_n + (X_n - x)\eta_{n-1}}{X_n - X_{n-1}} \qquad \text{for } (x,y) \in \mathcal{D}_n,\ n = 1,...,N. \tag{2.12}$$

Finally, the incident wave is given by

$$\phi^I(x,y,z) = e^{iK(x\cos\theta + y\sin\theta)} e^{Kz} \tag{2.13}$$

and the potentials ϕ^R and $\phi^D \equiv \phi^S - \phi^I$ describe outgoing waves at large distances from the raft.

In order to study the performance of the device we must first develop a description of its motion. It is possible to derive a system of equations in terms of the rotational and vertical motions of each of the individual pontoons. Indeed, this is the method used in [4] for a two-dimensional raft. These equations may then be solved for the unknown vertical velocities of the nodes η_n determining the right-hand-side of the kinematic condition (2.12). However, due to the mismatch of vertical and rotational parameterisations this leads to a somewhat untidy set of equations. Here, we instead describe the motion of the entire raft as the superposition of a set of generalised modes as advocated in [8].

3. Generalised Modes

We exploit the linearity of the governing equations to decompose the motion of the raft into the sum of $N+1$ linearly independent 'plate modes' (e.g. [8],[9]). Thus, we write the kinematic condition on the raft (2.12) as

$$\phi_z^R(x,y,0) = \sum_{n=0}^{N} U_n f_n(x) \tag{3.1}$$

where the functions $f_n(x)$ are prescribed functions forming a basis for the plate motion (defined later) and the coefficients U_n are unknown generalised velocities for $n = 0,...,N$. Correspondingly, we further decompose the radiation velocity potential, writing

$$\phi^R(x,y,z) = \sum_{n=0}^{N} U_n \phi_n(x,y,z) \tag{3.2}$$

where $\phi_n(x,y,z)$, for $n = 0,...,N$, represent radiation potentials associated with the forced motion of the raft in each of the $N+1$ modes and satisfy

$$\frac{\partial \phi_n}{\partial z}(x,y,0) = f_n(x) \qquad \text{for } (x,y) \in \mathcal{D}. \tag{3.3}$$

The generalised velocities used in this approach to describe the motion of the raft are determined by a set of equations of motion which will be outlined below.

3.1. Equations of Motion

The equations of motion of the articulated raft are written in terms of the generalised modes as

$$-i\omega \mathbf{M}\mathbf{U} = \mathbf{X}_S + (i\omega \mathbf{A} - \mathbf{B})\,\mathbf{U} + \mathbf{X}_e - \frac{i}{\omega}\mathbf{C}\mathbf{U} \tag{3.4}$$

where $\mathbf{X}_S$ is the exciting force vector with components given by

$$X_n^S = \rho g A \iint_{\mathcal{D}} \phi^S(x,y,0) f_n(x)\,dx\,dy \qquad \text{for } n = 0,...,N \tag{3.5}$$

and $\mathbf{A}$ and $\mathbf{B}$ are the real, symmetric added mass and radiation damping matrices associated with the radiation of waves with components defined by

$$i\omega A_{mn} - B_{mn} = i\omega\rho \iint_{\mathcal{D}} \phi_m(x,y,0) f_n(x)\,dx\,dy \qquad \text{for } n,m = 0,...,N. \tag{3.6}$$

Meanwhile, $\mathbf{C}$ and $\mathbf{M}$ encode the symmetric hydrostatic restoring and inertial forces, with elements given (e.g. [8]) by

$$C_{mn} = \rho g \iint_{\mathcal{D}} f_m(x) f_n(x)\,dx\,dy \quad \text{and} \quad M_{mn} = \rho_s h \iint_{\mathcal{D}} f_m(x) f_n(x)\,dx\,dy \quad \text{for } n,m = 0,...,N. \tag{3.7}$$

Finally, $\mathbf{X}_e$ is the vector of external mechanical torques due to the power take-off in the hinges, each having a real damping rate λ_n for $n = 1,...,N-1$. It is given by

$$\mathbf{X}_e = -\mathbf{D}\mathbf{U} \tag{3.8}$$

where $\mathbf{D}$ incorporates the power take-off parameters λ_n and depends on the choice of modes. Since we have not chosen to specify the functions $f_n(x)$ yet we cannot specify $\mathbf{D}$ at this stage: this will follow in section 3.2. However, we note that a choice of modes of motion in which at most one hinge is engaged by each mode would result in a diagonal matrix $\mathbf{D}$. This has advantages in the power take-off calculations of section 4 where we will consider the optimal tuning of the power take-off parameters.

Defining the the so-called impedance matrix

$$\mathbf{Z} = \mathbf{B} - i\omega\left(\mathbf{M} + \mathbf{A} - \mathbf{C}/\omega^2\right) \tag{3.9}$$

then allows us to rewrite the equation of motion (3.4) as

$$(\mathbf{D} + \mathbf{Z})\,\mathbf{U} = \mathbf{X}_S. \tag{3.10}$$

3.2. Choice of modes

There are various sensible choices which may be made for the modes of motion, each of which has its own benefits. One possible choice is a system of modes in which each node is

allowed to oscillate in turn whilst all others remain fixed, this is represented by the functions

$$f_n^k(x) = \frac{(x - X_{m-1})\delta_{m,n} - (x - X_m)\delta_{n,m-1}}{X_m - X_{m-1}} \qquad \text{when } x \in \mathcal{D}_m \text{ for } n = 0, ..., N \tag{3.11}$$

where $\delta_{m,n}$ is the Kronecker delta. This allows the algebraic connection between the generalised modes described above and the equations of motion formulated in [4] in terms of the rotational and vertical motions of each of the pontoons to be easily identified. Meanwhile, the choice of decomposition into symmetric and antisymmetric modes made by Newman in [7] for a system of three pontoons allows for optimal tuning of each mode and gives an insight into the contributions made by symmetric and antisymmetric motions. However, since the conditions on the power take-off parameters required for optimum performance in each of the two modes cannot in general be achieved simultaneously their sum produces a theoretical maximum instead of an achievable optimum for the power absorbed by the combined motion.

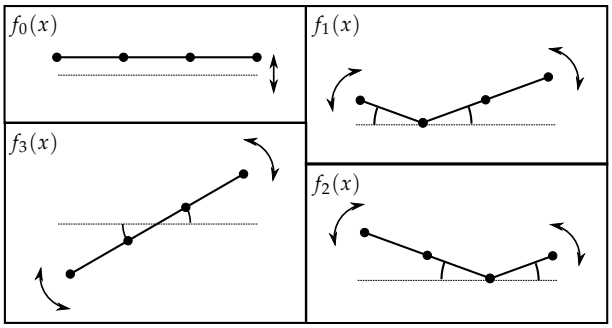

Figure 2: Illustration of 'plate modes' for a raft made up of three pontoons.

The choice which will be discussed in detail here is different to that proposed by Newman in [8] and suits our ultimate goal of assessing power. The rigid body modes associated with heave and pitch are isolated and each of the remaining $N - 1$ modes are chosen to engage just a single hinge. The two rigid body modes are represented by

$$f_0(x) = 1 \qquad \text{and} \qquad f_N(x) = x, \tag{3.12}$$

corresponding to heave and pitch respectively, whilst the remaining $N - 1$ hinged modes are given by

$$f_n(x) = |x - X_n| \qquad \text{for } n = 1, ..., N - 1. \tag{3.13}$$

For an illustration of the modes in the case of a raft made up of three pontoons, see Figure 2.

The generalised velocities associated with this choice of modes and contained within $\mathbf{U} = (U_0, ..., U_N)$, describe the vertical velocity in the heave mode for $n = 0$ and angular velocities associated with the hinged and pitching modes for $n = 1, ..., N$. Meanwhile, the key advantage of this choice is seen in the components of the vector of external mechanical torques $\mathbf{X}_e$ which are given by $X_{e,n} = -\lambda_n U_n$. Thus, since each bending mode engages just a single hinge, the power take-off is conveniently described by the diagonal matrix $\mathbf{D} = \text{diag}\{0, \lambda_1, ..., \lambda_{N-1}, 0\}$.

4. Power

Since we are interested in the performance of the raft as a wave energy converter our attention now turns to the time-averaged power absorption due to wave forces on the raft. This can be written as

$$W = \frac{1}{2}\Re\left\{\mathbf{X}_w^\dagger \mathbf{U}\right\} \tag{4.1}$$

where $\mathbf{X}_w = \mathbf{X}_S + (i\omega\mathbf{A} - \mathbf{B})\,\mathbf{U}$ is the wave force and the dagger denotes the conjugate transpose. Then, using (3.4) and noting that $\mathbf{C}$ and $\mathbf{M}$ are real and symmetric, we find

$$W = -\frac{1}{2}\Re\left\{\mathbf{X}_e^\dagger \mathbf{U}\right\} = \frac{1}{2}\mathbf{U}^\dagger \mathbf{D}\mathbf{U}, \tag{4.2}$$

the second equality resulting after substitution for the external mechanical torque from (3.8) since $\mathbf{D}$ is a real, diagonal matrix. Next, substituting for the velocity $\mathbf{U} = (\mathbf{Z} + \mathbf{D})^{-1}\,\mathbf{X}_S$ from (3.10) we gain

$$W = \frac{1}{2}\mathbf{X}_S^\dagger \mathbf{E}^\dagger \mathbf{D}\mathbf{E}\mathbf{X}_S \tag{4.3}$$

where $\mathbf{E} = (\mathbf{Z} + \mathbf{D})^{-1}$. Since the power take-off mechanism takes the form of mechanical damping in the hinges power is only absorbed in the $N-1$ bending modes and not in the rigid body modes. Despite this the elements in the expression for power given in (4.3) have dimension $N+1$. It is thus convenient to rearrange such that the rigid body modes correspond to the first two entries in any row or column. $\mathbf{E}$ may then be determined using a standard block matrix inversion formula (e.g. [1], (2.8.18)) resulting in the following expression for power

$$W = \frac{1}{2}\boldsymbol{\mathcal{X}}_S^\dagger \left(\boldsymbol{\mathcal{Z}}^\dagger + \boldsymbol{\Lambda}\right)^{-1} \boldsymbol{\Lambda}\,(\boldsymbol{\mathcal{Z}} + \boldsymbol{\Lambda})^{-1}\,\boldsymbol{\mathcal{X}}_S. \tag{4.4}$$

This process has resulted in an expression for power dependent on the full, diagonal power take-off matrix $\boldsymbol{\Lambda} = \mathrm{diag}(\lambda_1, ..., \lambda_{N-1})$. The elements of the matrix $\boldsymbol{\mathcal{Z}} = (\mathcal{Z}_{nm})$ are given by

$$\mathcal{Z}_{nm} = Z_{nm} - \frac{Z_{0n}Z_{0m}}{Z_{00}} - \frac{Z_{nN}Z_{mN}}{Z_{NN}} \qquad \text{for } n, m = 1, ..., N-1, \tag{4.5}$$

and the elements of the vector $\boldsymbol{\mathcal{X}}_S = (\mathcal{X}_n^S)$ are given by

$$\mathcal{X}_n^S = X_n^S - \frac{Z_{0n}}{Z_{00}}X_0^S - \frac{Z_{nN}}{Z_{NN}}X_N^S \qquad \text{for } n = 1, ..., N-1 \tag{4.6}$$

in which cursive capitals have been used to identify the newly defined matrices and their elements. The matrix size has thus been reduced from $N+1$ in (4.3) to $N-1$ in (4.4) reflecting the fact that the two rigid body modes do not contribute to power.

Differentiating (4.4) with respect to λ_i and setting it equal to zero for $i = 1, ..., N$ results in a system of N non-linear equations for λ_i, $i = 1, ..., N$. These equations determine the optimal values for the power take-off in the hinges, λ_i, $i = 1, ..., N$. In general these equations must be solved numerically. However, further analytic progress may be made in two particular cases. The first is a system of two identical pontoons with a single hinge and the second is a system of three symmetrically configured pontoons with identical power take-off in both hinges. When considering the factors that play a role in device performance it is sensible to start with the simplest configuration and build up the picture from there. The analytic results that follow will be very useful for efficiently assessing device performance in the early stages of this process.

4.1. Case N=2: two pontoons

In the particular case of two identical pontoons with a single hinge then (4.4) gives

$$W = \frac{1}{2}\frac{\lambda_1 |\mathcal{X}_1^S|^2}{|\mathcal{Z}_{11} + \lambda_1|^2}. \tag{4.7}$$

After using the identity $|\lambda_1 + \mathcal{Z}_{11}|^2 = 2\lambda_1\left(\Re\{\mathcal{Z}_{11}\} + |\mathcal{Z}_{11}|\right) + \left(\lambda_1 - |\mathcal{Z}_{11}|\right)^2$ this may be rewritten as

$$W = \frac{\left|\mathcal{X}_1^S\right|^2}{4(\Re\left\{\mathcal{Z}_{11}\right\} + |\mathcal{Z}_{11}|)}\left(1 - \frac{(\lambda_1 - |\mathcal{Z}_{11}|)^2}{|\lambda_1 + \mathcal{Z}_{11}|^2}\right). \tag{4.8}$$

By inspection we may then see that the raft is optimally tuned when $\lambda_1 = |\mathcal{Z}_{11}|$ and so

$$W_{opt} = \frac{|\mathcal{X}_1^S|^2}{4(\Re\{\mathcal{Z}_{11}\} + |\mathcal{Z}_{11}|)}. \tag{4.9}$$

This is then maximised when $\Im\{\mathcal{Z}_{11}\} = 0$, a condition which is determined by hydrodynamics alone and gives

$$W_{max} = \frac{|\mathcal{X}_1^S|^2}{8\Re\{\mathcal{Z}_{11}\}}. \tag{4.10}$$

If the maximum is achieved when $\omega = \omega^*$ then setting the damping to $\lambda_1 = B_{11} - B_{01}^2/B_{00} - B_{N1}^2/B_{NN}$ ensures the maximum power is extracted at $\omega = \omega^*$.

4.2. Case N=3: three pontoons

In the case of three symmetrically configured pontoons with two hinges and uniform power take-off parameters $\lambda_1 = \lambda_2 \equiv \lambda$, then we may extend the results of [11], for an array of two identical surging wave energy devices, to give

$$W = \frac{\lambda}{2}\left(\frac{|\mathcal{X}_1^S + \mathcal{X}_2^S|^2}{|\mathcal{Z}_{11} + \mathcal{Z}_{12} + \lambda|^2} + \frac{|\mathcal{X}_1^S - \mathcal{X}_2^S|^2}{|\mathcal{Z}_{11} - \mathcal{Z}_{12} + \lambda|^2}\right). \tag{4.11}$$

This is equivalent to a decomposition into symmetric and antisymmetric modes. Writing

$$f_\pm(x) = \begin{cases} \pm|x - X_1| & \text{for } X_0 < x < X_1 \\ 0 & \text{for } X_1 < x < X_2 \\ |x - X_2| & \text{for } X_2 < x < X_3 \end{cases} \tag{4.12}$$

then we find that $\mathcal{X}_\pm^S = (\mathcal{X}_2^S \pm \mathcal{X}_1^S)/2$ and $\mathcal{Z}_\pm = (\mathcal{Z}_{11} \pm \mathcal{Z}_{22})/2$ and so (4.11) may be rewritten as

$$\begin{aligned} W &= \frac{\lambda}{2}\left(\frac{|\mathcal{X}_+^S|^2}{|\mathcal{Z}_+ + \lambda/2|^2} + \frac{|\mathcal{X}_-^S|^2}{|\mathcal{Z}_- + \lambda/2|^2}\right) \\ &= \frac{|\mathcal{X}_+^S|^2}{4(\Re\{\mathcal{Z}_+\} + |\mathcal{Z}_+|)}\left(1 - \frac{(\lambda/2 - |\mathcal{Z}_+|)^2}{|\lambda/2 + \mathcal{Z}_+|^2}\right) + \frac{|\mathcal{X}_-^S|^2}{4(\Re\{\mathcal{Z}_-\} + |\mathcal{Z}_-|)}\left(1 - \frac{(\lambda/2 - |\mathcal{Z}_-|)^2}{|\lambda/2 + \mathcal{Z}_-|^2}\right) \end{aligned} \tag{4.13}$$

where the second line results after substituting for $|\lambda/2 + \mathcal{Z}_\pm|$ as in (4.8). The optimal tuning in the symmetric and antisymmetric modes is thus given by $\lambda = 2|\mathcal{Z}_+| = |\mathcal{Z}_{11} + \mathcal{Z}_{22}|$ and $\lambda = 2|\mathcal{Z}_-| = |\mathcal{Z}_{11} - \mathcal{Z}_{22}|$ respectively. Optimal tuning of the entire system is a compromise between the antisymmetric and symmetric modes resulting in bounds on the optimal power take-off parameter being given by

$$\min\{|\mathcal{Z}_{11} + \mathcal{Z}_{12}|, |\mathcal{Z}_{11} - \mathcal{Z}_{12}|\} \le \lambda_{opt} \le \max\{|\mathcal{Z}_{11} + \mathcal{Z}_{12}|, |\mathcal{Z}_{11} - \mathcal{Z}_{12}|\}. \tag{4.14}$$

Unfortunately, there aren't any cases in which this can be found exactly since the physical set up doesn't allow us to prescribe $\mathcal{X}_1^S = \pm\mathcal{X}_2^S$ unless $\theta = \pi/2$ in which case $\mathcal{X}_1^S = \mathcal{X}_2^S \equiv 0$ and there is no power absorption anyway. However, in practice the bounds are fairly tight and may be used to either approximate the optimum damping or accelerate its determination through numerical optimisation.

A typical example of the bounds on λ given in (4.14) is shown in figure 3, results having been computed using the solution method which follows in sections 5 and 6. $|\mathcal{Z}_{11} - \mathcal{Z}_{12}|$ (short dashed line), $|\mathcal{Z}_{11} + \mathcal{Z}_{12}|$ (long dashed line) and λ_{opt} as computed using an optimisation procedure (crosses) are plotted as a function of Ka in figure 3(a). We see that the numerical optimum

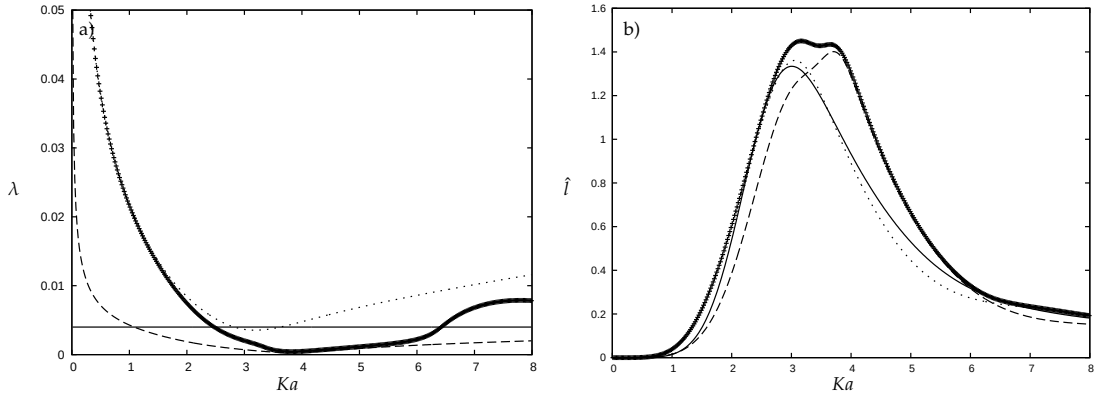

Figure 3: Figures demonstrate the bounds on the optimum power take-off. In figure (a) we see the power take-off parameter, λ and in (b) the capture factor, $\hat{l}$, each plotted as a function of Ka. Results are shown for a system of three equally sized pontoons with $a/b = 3$ and $d/2b = 0.15$. The crosses show results computed using an optimisation procedure to find optimal λ at each incident wave frequency whilst the dashed and dotted lines show lower and upper bounds on optimal λ. The solid line shows results for a particular, fixed value of λ which has been chosen to fit within the bounds as much as possible.

clearly lies within the analytic bounds for the full range frequencies. A particular, fixed value of λ (solid line) is also chosen by eye to lie within the bounds for a broad range of frequencies. Figure 3(b) plots the capture factors achieved by setting λ to the different values shown in figure (a) with line styles chosen correspondingly. We see that since the bounds on λ are fairly tight the capture factor computed using the single fixed value of λ (solid line) lies fairly close to the numerical optimum, making this a good way to either choose a fixed λ directly or to accelerate the numerical optimisation by providing tight bounds.

The choice of symmetric and antisymmetric modes used here is related to that made by Newman in [7]. In Newman [7] this provided a useful insight into the role played by the symmetric and antisymmetric modes and was also used to provide a theoretical upper bound on the maximum power absorption, W_{max}. This was determined by superposition of theoretical maximum power absorption achieved in each of the symmetric and antisymmetric modes. The tuning and resonance conditions required to achieve maximum power absorption were not considered. Here, we have shown that the conditions required for optimum power absorption in each of the modes cannot be simultaneously satisfied except where there is no available power. Thus, we instead consider a compromise between the optimum power absorption in each mode, providing tight bounds on the optimum power take-off parameter λ for the entire system.

5. Derivation of integral equations

Advantage can be taken of the recent work of Porter [13] and the mathematical techniques proposed therein for the solution of problems involving rigid plates lying on the surface of the water are extended here.

5.1. The scattering problem

The scattering problem deals with the diffraction of the incident wave by a fixed, horizontal raft and thus the solution in this case is simply an application of [13]. This gives an integral representation for $\phi^S(x,y,z)$,

$$\phi^S(x,y,z) = \phi^I(x,y,z) + \frac{K}{4\pi^2}\int_{-\infty}^{\infty}\int_{-\infty}^{\infty}\frac{\overline{P}(\alpha,\beta)}{K-k}e^{i\alpha x}e^{i\beta y}e^{kz}\,d\alpha\,d\beta, \tag{5.1}$$

where $k = \sqrt{\alpha^2 + \beta^2}$ and

$$\overline{P}(\alpha, \beta) = \iint_{\mathcal{D}} \phi^S(x, y, 0) e^{-i\alpha x} e^{-i\beta y} \, dx \, dy. \tag{5.2}$$

Then, setting $z = 0$ results in an integral equation for $\phi^S(x, y, 0)$,

$$\phi^S(x, y, 0) + \left(\mathcal{K}\phi^S\right)(x, y, 0) = e^{iK(x\cos\theta_0 + y\sin\theta_0)} \qquad \text{for } (x, y) \in \mathcal{D}, \tag{5.3}$$

where

$$\left(\mathcal{K}\phi\right)(x, y, 0) = \frac{1}{4\pi^2} \int_{-\infty}^{\infty} \int_{-\infty}^{\infty} \frac{K}{k - K} \iint_{\mathcal{D}} \phi(x', y', 0) e^{-i\alpha x'} e^{-i\beta y'} \, dx' \, dy' \, e^{i\alpha x} e^{i\beta y} \, d\alpha \, d\beta. \tag{5.4}$$

220 *5.2. The radiation Problem*

The solution method for the radiation problem is an extension of the above with the forcing provided by the incident wave being replaced by the forced oscillatory motions of the raft. We outline the mathematical development in more detail in the following. First, we define the Fourier transform of $\phi_n(x, y, z)$ by

$$\overline{\phi}_n(\alpha, \beta, z) = \int_{-\infty}^{\infty} \int_{-\infty}^{\infty} \phi_n(x, y, z) e^{-i\alpha x} e^{-i\beta y} \, dx \, dy \qquad \text{for } n = 0, ..., N. \tag{5.5}$$

Then, taking Fourier transforms of (2.8) and (2.9), it follows that

$$\left(\frac{d^2}{dz^2} - k^2\right) \overline{\phi}_n(\alpha, \beta, z) = 0 \qquad \text{for } z < 0 \tag{5.6}$$

where k is defined as in the scattering problem above and $\overline{\phi}_n \to 0$ as $z \to -\infty$ for $n = 0, ..., N$. Using (2.10) and (3.3) the kinematic and free surface conditions combine to give

$$\left(\frac{d}{dz} - K\right) \overline{\phi}_n(\alpha, \beta, 0) = \overline{I}_n(\alpha, \beta) - K\overline{P}_n(\alpha, \beta) \qquad \text{for } n = 0, ..., N. \tag{5.7}$$

where

$$\overline{P}_n(\alpha, \beta) = \iint_{\mathcal{D}} \phi_n(x, y, 0) e^{-i\alpha x} e^{-i\beta y} \, dx \, dy \tag{5.8}$$

and

$$\overline{I}_n(\alpha, \beta) = \iint_{\mathcal{D}} \frac{\partial \phi_n}{\partial z}(x, y, 0) e^{-i\alpha x} e^{-i\beta y} \, dx \, dy = \iint_{\mathcal{D}} f_n(x) e^{-i\alpha x} e^{-i\beta y} \, dx \, dy. \tag{5.9}$$

Thus, we find that the Fourier transformed velocity potential is given by

$$\overline{\phi}_n(\alpha, \beta, z) = \frac{\overline{I}_n(\alpha, \beta) - K\overline{P}_n(\alpha, \beta)}{k - K} e^{kz} \qquad \text{for } n = 0, ..., N. \tag{5.10}$$

Invoking the inverse Fourier transform of (5.10) then results in an integral representation for $\phi_n(x, y, z)$,

$$\phi_n(x, y, z) = \frac{1}{4\pi^2} \int_{-\infty}^{\infty} \int_{-\infty}^{\infty} \frac{\overline{I}_n(\alpha, \beta) - K\overline{P}_n(\alpha, \beta)}{k - K} e^{i\alpha x} e^{i\beta y} e^{kz} \, d\alpha \, d\beta \qquad \text{for } n = 0, ..., N. \tag{5.11}$$

Setting $z = 0$, as before, we gain a set of integral equations for $\phi_n(x, y, 0)$ for $n = 0, ..., N$,

$$\phi_n(x, y, 0) + \left(\mathcal{K}\phi_n\right)(x, y, 0) = \frac{1}{4\pi^2} \int_{-\infty}^{\infty} \int_{-\infty}^{\infty} \frac{\overline{I}_n(\alpha, \beta)}{k - K} e^{i\alpha x} e^{i\beta y} \, d\alpha \, d\beta, \qquad \text{for } (x, y) \in \mathcal{D} \tag{5.12}$$

where $\mathcal{K}$ was defined in (5.4).

6. Solution of integral equations

To access numerical solutions of (5.3) and (5.12) we employ a Galerkin expansion method. We thus expand the unknown functions associated with the scattered waves in terms of a complete set of orthogonal basis functions

$$\phi^S(x,y,0) \simeq \sum_{p=0}^{\infty}\sum_{r=0}^{\infty} c_{pr}^S v_p\left(\frac{x}{a}\right) v_r\left(\frac{y}{b}\right) \tag{6.1}$$

for $n = 0, ..., N$ where $v_r(t) = \frac{1}{2}e^{ir\pi/2}P_r(t)$ and $P_r(t)$ are orthogonal Legendre polynomials satisfying

$$\int_{-1}^{1} P_r(t)P_s(t)\,dt = \frac{2\delta_{r,s}}{2r+1} \qquad \text{and} \qquad \int_{-1}^{1} P_r(t)e^{-i\sigma t}\,dt = 2e^{-ir\pi/2}j_r(\sigma), \tag{6.2}$$

where $j_r(\sigma)$ denote Spherical Bessel functions. This choice of orthogonal Legendre polynomials is identical to that made in [13]. This is not the only possible choice of basis functions, we could have used Fourier series for example, but Legendre polynomials provide the maximum simplification in the numerical system. Substituting for this expansion in the integral equation (5.3), multiplying through by $v_q^*(x/a)v_s^*(y/b)$ and integrating over $(x,y) \in \mathcal{D}$ results in the following system of linear equations

$$\frac{c_{qs}^S}{4(2q+1)(2s+1)} + \sum_{p=0}^{\infty}\sum_{r=0}^{\infty} c_{pr}^S K_{pqrs} = D_{qs}^S \qquad \text{for } s,q = 0,1,2,.... \tag{6.3}$$

Using a similar expansion for $\phi_n(x,y,0)$ in which the coefficients in (6.1) are replaced by $4ac_{pr}^{(n)}$ then results in

$$\frac{c_{qs}^{(n)}}{4(2q+1)(2s+1)} + \sum_{p=0}^{\infty}\sum_{r=0}^{\infty} c_{pr}^{(n)} K_{pqrs} = D_{qs}^{(n)} \qquad \text{for } s,q = 0,1,2,... \text{ and } n = 0,...,N \tag{6.4}$$

where

$$K_{pqrs} = \frac{Kab}{4\pi^2}\int_{-\infty}^{\infty}\int_{-\infty}^{\infty} \frac{j_p(\alpha a)j_q(\alpha a)j_r(\beta b)j_s(\beta b)}{k-K}\,d\alpha\,d\beta, \tag{6.5}$$

whilst

$$D_{qs}^S = j_q(Ka\cos\theta)j_s(Kb\sin\theta) \tag{6.6}$$

and

$$D_{qs}^{(n)} = \frac{Kab}{4\pi^2}\int_{-\infty}^{\infty}\int_{-\infty}^{\infty} \frac{j_q(\alpha a)j_s(\beta b)j_0(\beta b)}{k-K}F_n(\alpha a)\,d\alpha\,d\beta \quad \text{with} \quad F_n(t) = \frac{1}{2Ka}\int_{-1}^{1} f_n(a\zeta)e^{-i\zeta t}\,d\zeta \tag{6.7}$$

for $n = 0, ..., N$. We note that the right-hand side of (6.4) is of a similar form to the integral K_{pq0s} only with the replacement $j_p(\alpha a) \to F_n(\alpha a)$.

Due to the symmetries of the integrand K_{pqrs} vanishes if either $p+q$ or $r+s$ is odd. This redundancy results in the reduction of (6.3) to a set of four uncoupled systems of linear equations

$$\frac{c_{2q+\nu,2s+\mu}^S}{4(4q+2\nu+1)(4s+2\mu+1)} + \sum_{p=0}^{\infty}\sum_{r=0}^{\infty} c_{2p+\nu,2r+\mu}^S K_{2p+\nu,2q+\nu,2r+\mu,2s+\mu} = D_{2q+\nu,2s+\mu}^S \tag{6.8}$$

for $s, q = 0, 1, 2, ...$ and $\nu, \mu = 0, 1$ whilst (6.4) is similarly reduced to a set of two uncoupled systems of linear equations

$$\frac{c^{(n)}_{2q+\nu,2s}}{4(4q+2\nu+1)(4s+1)} + \sum_{p=0}^{\infty}\sum_{r=0}^{\infty} c^{(n)}_{2p+\nu,2r} K_{2p+\nu,2q+\nu,2r,2s} = D^{(n)}_{2q+\nu,2s} \tag{6.9}$$

for $s, q = 0, 1, 2, ...$, $\nu = 0, 1$ and $n = 0, ..., N$ where

$$K_{2p+\nu,2q+\nu,2r+\mu,2s+\mu} = \frac{Kab}{\pi^2}\int_0^{\infty}\int_0^{\infty} \frac{j_{2p+\nu}(\alpha a) j_{2q+\nu}(\alpha a) j_{2r+\mu}(\beta b) j_{2s+\mu}(\beta b)}{k - K}\, d\alpha\, d\beta, \tag{6.10}$$

along with

$$D_{2q+\nu,2s+\mu} = j_{2q+\nu}(Ka\cos\theta) j_{2s+\mu}(Kb\sin\theta) \tag{6.11}$$

and

$$D^{(n)}_{2q+\nu,2s} = \frac{Kab}{2\pi^2}\int_0^{\infty}\int_0^{\infty} \frac{j_{2q+\nu}(\alpha a) j_{2s}(\beta b) j_0(\beta b)}{k - K} \left(F_n(\alpha a) + (-1)^{\nu} F_n(-\alpha a)\right)\, d\alpha\, d\beta. \tag{6.12}$$

7. Numerical Calculations

7.1. Numerical computation of integrals and truncation of infinite summations

For computational purposes it is convenient to express the functions $f_n(x)$ in terms of the Legendre polynomial basis functions when evaluating $F_n(\alpha a)$. Using the first two Legendre polynomials, $P_0(x) = 1$ and $P_1(x) = x$, the rigid body modes may be written as

$$f_0(x) = 2v_0\left(\frac{x}{a}\right) \qquad \text{and} \qquad f_N(x) = -iav_1\left(\frac{x}{a}\right) \tag{7.1}$$

whilst the bending modes defined in (3.13) may be expressed using more complicated arguments as

$$f_n(x) = \begin{cases} (X_n + a)\left[v_0\left(\frac{2x+(a-X_n)}{X_n+a}\right) + iv_1\left(\frac{2x+(a-X_n)}{X_n+a}\right)\right] & \text{if } x \le X_n \\ (a - X_n)\left[v_0\left(\frac{2x-(X_n+a)}{a-X_n}\right) - iv_1\left(\frac{2x-(X_n+a)}{a-X_n}\right)\right] & \text{if } x \ge X_n \end{cases} \tag{7.2}$$

for $n = 1, ..., N-1$. Thus,

$$F_n(\alpha a) = \begin{cases} \frac{1}{Ka} j_0(\alpha a) & \text{for } n = 0 \\ \frac{-i}{2K} j_1(\alpha a) & \text{for } n = N \end{cases} \tag{7.3}$$

and

$$\begin{aligned} F_n(\alpha a) = \frac{1}{4Ka^2}\Big[&(X_n + a)^2 e^{-i\alpha(a-X_n)/2}\left(j_0\left(\alpha(a+X_n)/2\right) + ij_1\left(\alpha(a+X_n)/2\right)\right) \\ &+ (X_n - a)^2 e^{-i\alpha(a+X_n)/2}\left(j_0\left(\alpha(a-X_n)/2\right) - ij_1\left(\alpha(a-X_n)/2\right)\right)\Big] \end{aligned}$$

for $n = 1, ..., N-1$. This allows us to express the integrals defining $D^{(n)}_{qs}$ in terms of a linear combination of trigonometric functions and spherical Bessel functions of more complicated arguments.

In order to evaluate the integrals defining K_{pqrs} and $D^{(n)}_{qs}$ numerically we follow the numerical methods outlined in [13] leading to principal-value integrals which decay like $O(1/k^4)$. The numerical systems also converge rapidly and infinite summations are truncated at $p = q = 2P + 1$ and $r = s = 2R + 1$ for the sake of numerical computation. Numerical experimentation suggests that as few as $P = R = 5$ modes in the Galerkin approximation are sufficient to produce results which are accurate enough for graphical purposes in all results presented.

For comparison, panel methods numerical codes would require in the order of $N = 1000 - 10,000$ panels for a large structure [12] and the numerical effort would be of order N^3. In contrast, the developed here is a spectral method which requires inversion of systems of equations between $N = 10 - 100$ in size, although there is also numerical effort involved in calculating matrix elements. A direct comparison of numerical effort has not been assessed.

7.2. The Response Amplitude Operator

The formulation is based on a linearised theory of water waves and there has been an *a priori* assumption that excursions of the raft from its equilibrium position are small in order that the results retain validity. We must therefore be careful to ensure that this assumption is justified in the results presented. To do this we consider the size of the response of nth node, given in terms of the generalised modes of motion as

$$\eta_n = \sum_{m=0}^{N} U_m f_m(X_n) = \mathbf{f}^T(X_n)\mathbf{U}. \tag{7.4}$$

We recall from (3.10) that

$$\mathbf{U} = (\mathbf{D} + \mathbf{Z})^{-1}\,\mathbf{X}_S \tag{7.5}$$

and so, since from (2.7) the maximum vertical excursion of the nth node for a particular incident wave frequency is given by $|\zeta_n| = |\eta_n/\omega|$, we have

$$\left|\frac{\zeta_n}{H}\right| = \frac{|\eta_n|}{H\omega} = \frac{\left|\mathbf{f}^T(X_n)\,(\mathbf{D} + \mathbf{Z})^{-1}\,\mathbf{X}_S\right|}{H\omega}, \tag{7.6}$$

the (dimensional) measure of the maximum vertical displacement of the nth node per unit height of incident wave. This is termed the RAO or response amplitude operator.

7.3. The physical parameters of the device

We define the following matrices of dimensionless quantities

$$\hat{\mathbf{A}} = \frac{\mathbf{M}_w^{-1}\mathbf{A}\mathbf{M}_w^{-1}}{16\rho a^2 b}, \qquad \hat{\mathbf{B}} = \frac{\mathbf{M}_w^{-1}\mathbf{B}\mathbf{M}_w^{-1}}{16\rho\omega a^2 b}, \qquad \text{and} \qquad \hat{\mathbf{D}} = \frac{\mathbf{M}_w^{-1}\mathbf{D}\mathbf{M}_w^{-1}}{16\rho\omega a^2 b} \tag{7.7}$$

where $\mathbf{M}_w = \text{diag}\,(M_{w,n})$ is the matrix with diagonal elements given by $M_{w,0} = 1$ and $M_{w,n} = a$ for $n = 1, ..., N$. Thus, the impedance is represented by

$$\hat{\mathbf{Z}} = \frac{\mathbf{M}_w^{-1}\mathbf{Z}\mathbf{M}_w^{-1}}{16\rho\omega a^2 b} \tag{7.8}$$

whilst the dimensionless exciting force is given by

$$\hat{\mathbf{X}}_S = \frac{\mathbf{M}_w^{-1}\mathbf{X}_S}{16\rho g A a b}. \tag{7.9}$$

To determine a measure of the effectiveness of the device we also need to normalise the power. In order to do this we use the capture width of the wave energy converter. This is defined by

$$l = \frac{W}{W_{inc}} \tag{7.10}$$

for an incident wave $W_{inc} = \rho g|A|^2/4K$ and represents the equivalent crest length of incident wave from which all the energy has been absorbed. This still has the dimensions of length, so for the purpose of results we use the so-called capture factor, which is further non-dimensionalised

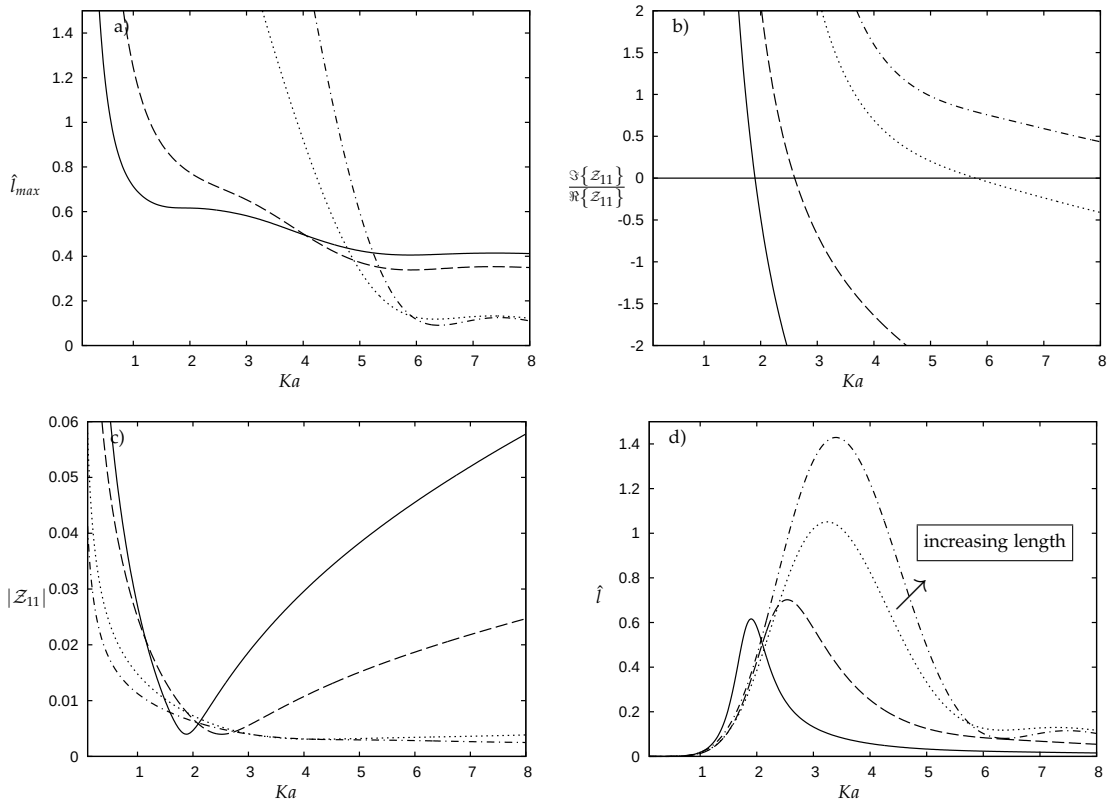

Figure 4: The figures show (a) the maximum capture factor $\hat{l}_{max}$, (b) the condition for resonance $\Im\{\mathcal{Z}_{11}\}/\Re\{\mathcal{Z}_{11}\}$, (c) the condition for tuning $|\mathcal{Z}_{11}|$ and (d) a realisation of the capture factor $\hat{l}$ with λ tuned to the peak of $\hat{l}_{opt}$. Results correspond to a system of two pontoons with a centrally positioned hinge and $d/2b = 0.125$ fixed along with $a/b = 0.5$ (solid line), 1 (dashed line), 5 (dotted line) and 10 (chained line).

by the width of the device

$$\hat{l} = l/2b \tag{7.11}$$

Thus, for a value of $\hat{l}$ greater than one then wave energy is absorbed from beyond the wave frontage on the device.

A uniform power take-off $\lambda_1 = \lambda_2 = ... \equiv \lambda$ will be used throughout results as little improvement was seen when greater freedom was allowed. In addition, a specific gravity of 0.5 is chosen to be physically reasonable and numerical experimentation with this parameter has shown it to have little qualitative effect.

8. Results

In this paper we have applied and extended the mathematical techniques proposed by Porter in [13] for problems involving rigid plates wherein results for rigid body modes have been validated. In a subsequent paper by the authors [10] results for power absorption, dependent on the hinged modes, are compared to various limiting approximations. Good agreement with two-dimensional and slender body results is seen for limiting aspect ratios along with rapid convergence to a continuously-flexible model with increasing N.

Since the focus of the present paper is on the energy absorbing capacity of the articulated raft wave energy converter our attention now turns to the capture factor, $\hat{l}$, defined by (7.11). Throughout the results we will explore the different factors which play a role in the success of raft-type devices, from the device proportions to hinge positioning and the number of constituent pontoons. To this end, we begin to build up our picture with the simplest case of two

pontoons connected via a single hinge. In this case we have analytic results for optimum and maximum power take-off as discussed in section 4.1. This allows us to get a clear idea of how the pontoon dimensions and hinge position impact performance.

There are three key ingredients in the determination of the capture factor for a single hinged raft. First the upper bound set by $\hat{l}_{max}$, which (from (4.10)) is given by

$$\hat{l}_{max} = \frac{|\mathcal{X}_1^S|^2}{16b\Re\{\mathcal{Z}_{11}\}W_{inc}}. \tag{8.1}$$

This wants to be as high as possible and depends on the exciting force so is key to directionality. Second,

$$\frac{2\Re\{\mathcal{Z}_{11}\}}{\Re\{\mathcal{Z}_{11}\}+|\mathcal{Z}_{11}|} = \frac{2}{1+\sqrt{1+(\Im\{\mathcal{Z}_{11}\}/\Re\{\mathcal{Z}_{11}\})^2}} \tag{8.2}$$

which determines resonance, multiplying $\hat{l}_{max}$ to set $\hat{l}_{opt}$. Clearly this wants to be as close to unity as possible, something which may be achieved by minimising the factor $\Im\{\mathcal{Z}_{11}\}/\Re\{\mathcal{Z}_{11}\}$; resonance occurs when this is equal to zero. The final factor to play a part is

$$1-\frac{(\lambda-|\mathcal{Z}_{11}|)^2}{|\lambda+\mathcal{Z}_{11}|^2} \tag{8.3}$$

which incorporates the power take-off parameter λ. This describes the tuning of the device and multiplies $\hat{l}_{opt}$ to set $\hat{l}$, the actual capture factor which may be achieved for a fixed value of λ. Optimal tuning requires $\lambda = |\mathcal{Z}_{11}|$ and in general we want $|\mathcal{Z}_{11}|$ to vary as little as possible to allow for broad-banded tuning.

We begin by considering the optimum device dimensions. In figure 4, the elements which play a role in power absorption are illustrated for a variety of pontoon proportions in the simplest case of a two pontoon system with a centrally positioned hinge. We vary the length to width ratio, considering $a/b = 0.5$, 1, 5 and 10 whilst the cross-sectional aspect ratio remains fixed at $d/2b = 0.125$, experimentation having shown little quantitative change as a result of varying this parameter within the small draught regime. Realisations of the capture factor tuned to the peak of $\hat{l}_{opt}$ are shown in 4(d). The capture factor $\hat{l}$ increases for large values of a/b with the peak exceeding 1 for long and narrow devices. This demonstrates the device's capacity to absorb power beyond that which is directly incident on its frontage. In order to understand the elements which play a role in this behaviour we turn our attention to figures 4(a)-(c). First, we examine the positioning of the resonant peak under the upper bound set by $\hat{l}_{max}$. Resonance is a key factor in wave energy converter design and we would like the device to be resonant where the upper bound is at its highest. However, comparison of figures 4(a) and (b) shows that for all aspect ratios resonance occurs at a much larger value of Ka, positioning the resonant peak beneath $\hat{l}_{max}$ where it is at its lowest. However, in the case of long devices the peak of the capture factor does not coincide with resonance. Instead an advantageous non-resonant peak in the optimum capture factor is seen for lower wave numbers, where the upper bound is higher. This is due to $\Im\{\mathcal{Z}_{11}\}/\Re\{\mathcal{Z}_{11}\}$ remaining small for values of Ka less than the resonant frequency resulting in a near-resonant effect. The other factor to play a part is the tuning. The raft is optimally tuned when $\lambda = |\mathcal{Z}_{11}|$, a quantity which is shown in figure 4(c). Large fluctuations are seen for short rafts, ruling out broad-banded tuning in this case, whilst for long rafts $|\mathcal{Z}_{11}|$ has a shallower gradient and $\hat{l}$ consequently sits close to $\hat{l}_{opt}$ for a broad range of frequencies. These factors combine to favour large values of a/b as seen in 4(d), though it is worth noting that this increase in power absorption is not proportionate to the increase in length and so a balance must be struck between the increase in capture factor and the device cost. For all subsequent results we select an average pontoon length corresponding to $a_n/2b = 2.5$ since this displays the beneficial behaviour of a longer device whilst also accounting for the increasing costs. For example, tuning the peak of figure 4(d) with $a/b = 10$ to an incident wave period $T = 9s$ would result in a raft 130m long and 26m wide with 3m draught.

Performance may be improved further by varying the hinge position. In figure 5(a)-(d)

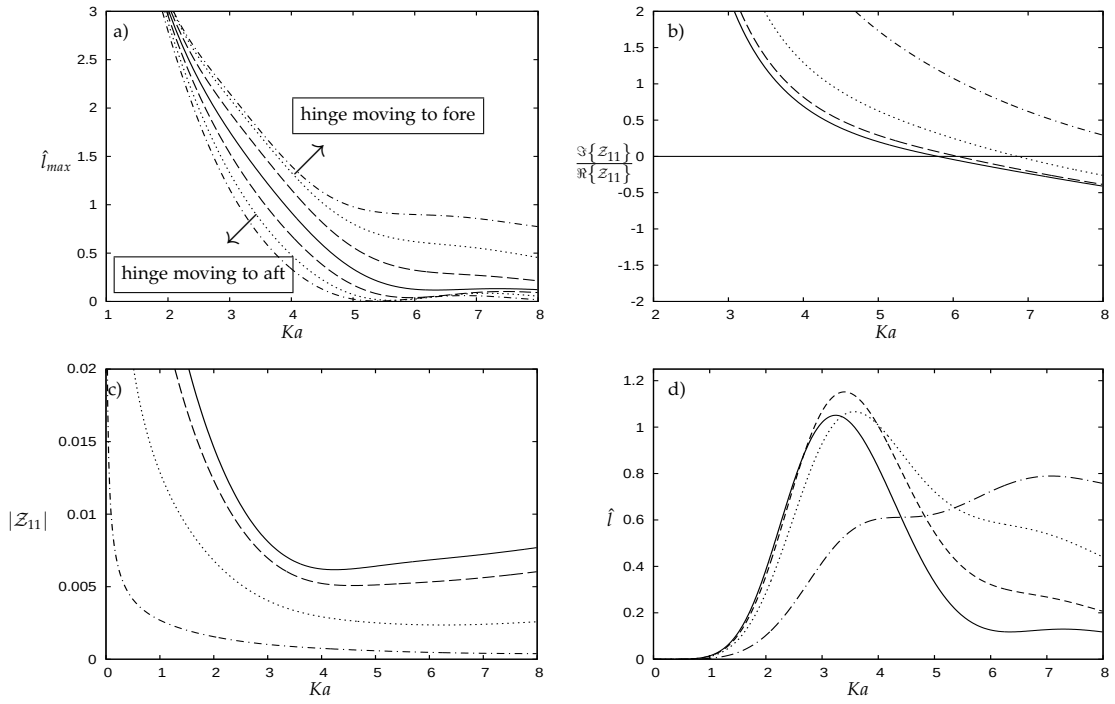

Figure 5: In all figures results are shown for $a/b = 5$ and $d/2b = 0.125$ whilst solid, dashed, dotted and chained curves correspond to pontoon ratios 1:1, 3:5, 2:6 and 1:7 respectively. Figures (a)-(c) show the effect of moving the hinge position on the maximum capture factor, resonance and tuning whilst figure (d) shows the actual capture factors for hinge positions forwards of centre when the raft is tuned to the peak of $\hat{l}_{opt}$.

results are shown for a system of two pontoons with a central hinge position (solid line) along with pontoon ratios 3:5 (dashed), 2:6 (dotted) and 1:7 (chained). The three key ingredients in the capture factor mentioned above are shown in figures 5(a-c) whilst the actual capture factors achievable for hinge positions forwards of centre are shown in figure (d). Realisations in which the raft is optimally tuned at the peak of $\hat{l}_{opt}$ have been selected for the purposes of illustration. The first ingredient, $\hat{l}_{max}$, is key to the directional bias of the asymmetry since it is the only point at which the exciting force plays a role. This upper bound increases as the hinge position moves towards the fore of the raft and decreases as it moves towards the aft. The second factor is shown in 5(b) and demonstrates resonance. The raft has the lowest resonant frequency when the hinge is positioned centrally with the resonant peak moving to higher wave numbers as the hinge position becomes increasingly asymmetric. For small asymmetries, like a 3:5 ratio, this effect is outweighed by the higher upper bound, but for more extremely asymmetric configurations it leads to a lower peak in $\hat{l}$. Finally, tuning is demonstrated in figure 5(c) and here the least variation is seen for the 1:7 pontoon ratio (the greatest asymmetry). It is clear that a shorter aft pontoon is universally detrimental to performance whilst some gains may be seen with a shorter fore. A relatively small introduction of asymmetry with the ratio 3:5 sees an overall improvement over the symmetric case whilst the benefit of more extreme ratios is seen mostly for larger values of Ka. Choosing the ideal pontoon ratio thus depends on the size of the raft relative to the incident wavelength (which sets Ka). For the purposes of the present work we decide to use the ratio 3:5 when considering hinge positioning for larger systems.

Based on the pontoon ratios investigated for two pontoons we now consider larger systems of 3 and 5 pontoons. Realisations of the capture factor tuned to the peak of the numerically determined optimum are plotted in figure 6(a) for a system of three pontoons. We consider the four configurations shown to scale in 6(b), all variations in pontoon size following a 3:5 ratio. Results follow the same pattern established for a single hinged raft with an overall improvement seen for the configuration with shorter pontoons positioned to the fore whilst positioning

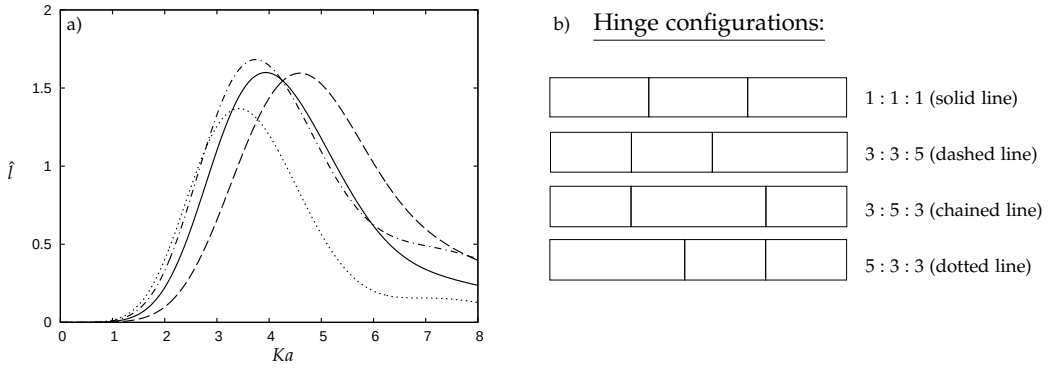

Figure 6: Results are shown for $a/b = 7.5$, $d/2b = 0.125$ and $N = 3$ fixed. All variations in pontoon size follow a 3:5 ratio. Solid, dotted, dashed and chained curves correspond to different configurations as shown in figure (b).

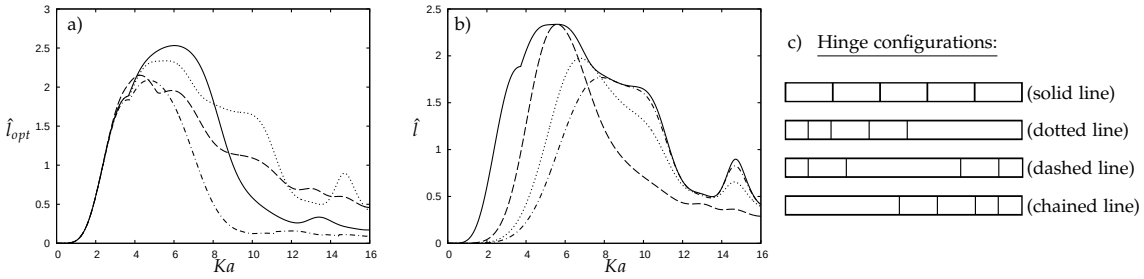

Figure 7: Results are shown for $a/b = 12.5$, $d/2b = 0.125$ and $N = 5$ fixed and all variations in pontoon size follow a 3:5 ratio. In figure (a) the optimum capture factor is plotted as a function of Ka for the various configurations shown in figure (c). In figure (b) the optimum capture factor $\hat{l}_{opt}$ corresponding to increasing pontoon length from fore to aft is then plotted (solid line) along with three realisations of $\hat{l}$ (dotted, dashed and chained lines).

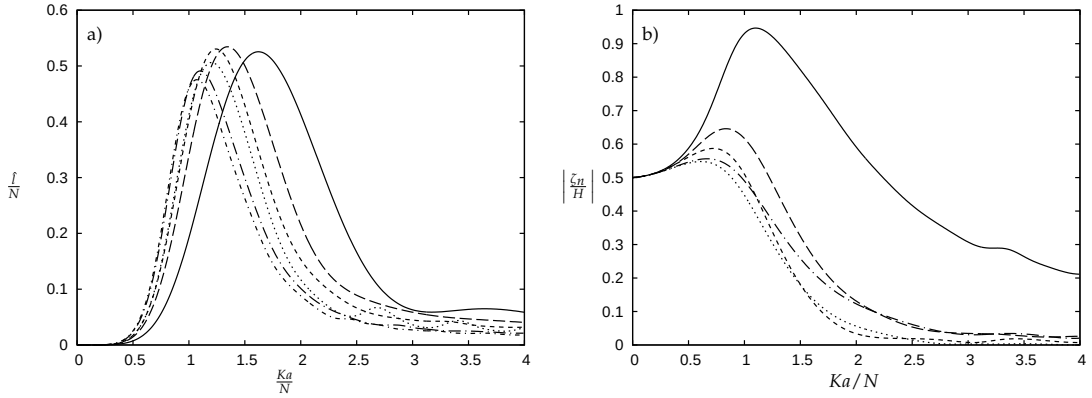

Figure 8: In figure (a) the normalised actual capture factor $\hat{l}/N$ is plotted against Ka/N for $a_n/2b = 2.5$ and $d/2b = 0.125$ fixed. Systems of $N = 2, 3, 4, 5, 6$ and 7 pontoons are shown by solid, long dashed, short dashed, dotted, long chained and short chained curves respectively. The power take-off parameter λ is tuned to the peak of the $\hat{l}_{opt}$. In figure (b) the corresponding average displacement per unit height of incident wave of the hinges and end-points $|\zeta_n/H|$ is shown for $n = 0$ (the fore end-point, solid curve), $n = 1, 2, 3$ (the hinges, long dashed, short dashed and dotted curves) and $n = 4$ (the aft end-point, chained curve) in the case when $N = 4$.

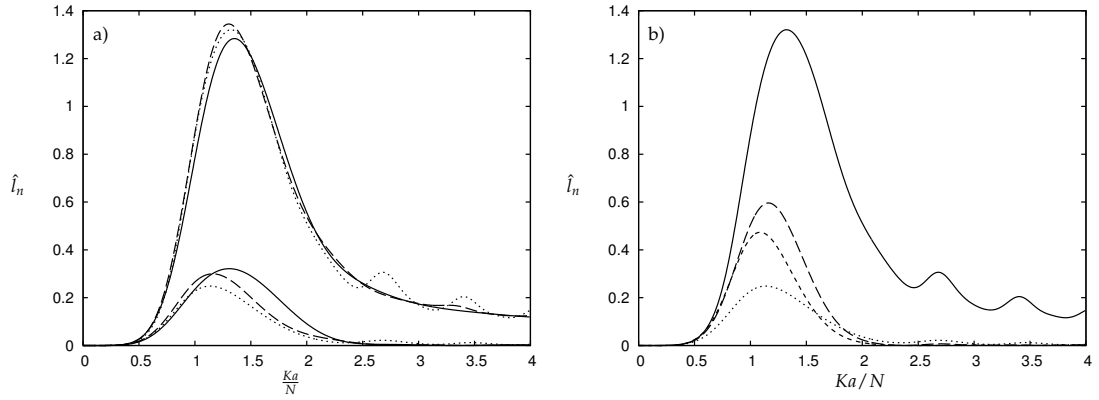

Figure 9: The capture factor due of the fore hinge $\hat{l}_1$ and the capture factor of the aft hinge $\hat{l}_{N-1}$ associated with systems of $N = 3, 4$ and 5 pontoons are plotted in figure (a). The solid, dashed and dotted line styles correspond to systems made up of $N = 3, 4$ and 5 pontoons respectively. Meanwhile, figure (b) shows the capture factor associated with each hinge for a system made up of $N = 5$ pontoons, $\hat{l}_n$ for $n = 1, .., 4$. Solid, long dashed, short dashed and dotted curves correspond to $\hat{l}_1$, $\hat{l}_2$, $\hat{l}_3$ and $\hat{l}_4$ respectively. In all cases $a_n/2b = 2.5$ and $d/2b = 0.125$ are fixed and the power take-off parameter λ is tuned to the peak of $\hat{l}_{opt}$.

shorter pontoons to the aft can be seen to be detrimental to performance. The symmetric configuration shifts to favour larger Ka, but is otherwise equivalent to equal sizing. In figure 7 we then consider hinge positioning for a system of 5 pontoons. The hinges are positioned so that all variations in pontoon sizing follow a 3:5 ratio. The optimum capture factor is shown as a function of Ka for a variety of configurations in figure 7(a). Again, decreasing pontoon length from fore to aft is universally detrimental to performance, the best results being seen with shorter pontoons positioned to the fore. Increasing pontoon length with a larger variations in sizing (three sizes within a single configuration, shown by the dotted line) we see a broad-banded response. The realisations shown in figure 7(b) demonstrate the potential to tune such a device to a variety of incident wave spectra.

Finally, we consider the effect of increasing the number of pontoons in the system. We fix the pontoon proportions at $a_n/2b = 2.5$ and $d/2b = 0.125$. Figure 8 shows the normalised actual capture factor $\hat{l}/N$, tuned to the peak of the optimum capture factor for systems of 2, 3, 4, 5, 6 and 7 pontoons. The capture factor can be seen to be of order N, the focusing effect of the raft drawing in waves from oblique angles towards the aft of the device. Thus, each additional pontoon contributes to power absorption equally, allowing the device the potential to absorb far more energy than that which is directly incident upon its frontage. This limitless increase in capture factor with length was also identified in [16] in which the maximum capture width W_{max}/W_{inc} for an attenuating line absorber was considered. The vertical excursions (or RAO) $|\zeta_n/H|$ were computed in all cases and are shown for the example of a system of 4 pontoons in figure 8(b). The peak displacement remains less than the incident wave height, validating the use of linear theory. The fore end-point undergoes a considerably larger maximum excursion than the hinges, the motion then being attenuated along the length of the raft until the tail end where a slight increase in excursion is seen as the remaining wave energy is transmitted beyond the device. This behaviour is consistent across all system sizes considered.

It is of interest to see how power absorption is divided between the hinges along the length of the device. To that end we consider the capture factor associated with each individual hinge $\hat{l}_n = W_n/(2bW_{inc})$ for $n = 1, ..., N-1$. Here, W_n is the power absorbed by each hinge and is given by the rate of working of the mechanical torque against the motion of the raft in the nth mode,

$$W_n = -\frac{1}{2}\Re\left\{X^*_{e,n}U_n\right\} = \frac{1}{2}\frac{\lambda_n|U_n|^2}{2bW_{inc}} \qquad \text{for } n = 1, ..., N-1, \tag{8.4}$$

in which the * notation denotes the complex conjugate. Figure 9(a) shows the behaviour of

the capture factor associated with fore and aft hinges, $\hat{l}_1$ and $\hat{l}_{N-1}$, with increasing N. We see that for $N = 3, 4$ and 5 pontoons there is little change in power absorption, with the fore hinge seeing a small improvement due to the addition of pontoons and the aft pontoon seeing a small deterioration. This behaviour continues for larger N. Meanwhile, the power absorption of the hinges along the length of the device in the 5 pontoon case is shown in figure 9(b). Here we see that the power absorption potential attenuates along the length of the device, with the largest contribution being made by the fore hinge and the smallest by the aft. Since the contributions to power due to the fore and aft hinges see little change with increasing pontoon number this results in the contribution to the capture factor due to the addition of pontoons consistently falling in the middle with its peak at $\hat{l}_n \simeq 0.5$. In all cases the power take-off parameter λ has been tuned to the peak of $\hat{l}_{opt}$ ($\hat{\lambda} = 0.000119/\sqrt{Kh}$ in the case of $N = 5$, for example).

9. Conclusions

In this paper we have developed an analytical approach to calculations assessing the performance of an articulated raft wave energy converter. The solution method is fully three-dimensional and this along with its high efficiency has allowed us to explore a large parameter space quickly and easily when considering the factors which play a role in the success of raft type converters. We have compared a wide variety of possible configurations rather than focusing on parameters specific to a particular design such as Pelamis or Cockerell's raft. Three significant factors are the device proportions, the hinge position and the number of pontoons of which the raft is comprised. A long, narrow raft has been shown to perform best, favouring an attenuator type raft design. Positioning the hinges such that pontoon length increases from fore to aft of the raft also has clear benefits whilst placing shorter pontoons to the aft is universally detrimental to performance. Relatively small deviations from equal pontoon sizing provide a small, but broad-banded improvement whilst greater variation in pontoon lengths allows for tuning to a multi-peaked spectrum. Finally, the number of pontoons used in the raft is of particular interest. In this paper we have shown the capture factor to be of order N for large rafts, thus demonstrating the capacity of a slender raft-type device to continue to absorb as much energy from the aft pontoon as the number of pontoons increases. This focusing effect is a cornerstone of the success of attenuator type devices and allows an articulated raft to absorb far more energy than that which is directly incident on its frontage.

Acknowledgement

I.F. Noad wishes to acknowledge the receipt of a University of Bristol Postgraduate Research Scholarship.

References

[1] Bernstein, D. S. (2009). *Matrix mathematics: theory, facts, and formulas*. Princeton University Press.

[2] Cockerell, C., Platts, M., and Comyns-Carr, R. (1978). The development of the wave-contouring raft. In *Wave energy conference. Abstracts of papers*.

[3] Evans, D., Jeffrey, D., Salter, S., and Taylor, J. (1979). Submerged cylinder wave energy device: theory and experiment. *Applied Ocean Research*, 1(1):3–12.

[4] Haren, P. and Mei, C. C. (1979). Wave power extraction by a train of rafts: hydrodynamic theory and optimum design. *Applied Ocean Research*, 1(3):147–157.

[5] Mei, C. C. and Newman, J. N. (1979). Wave power extraction by floating bodies. Technical report, DTIC Document.

[6] Moody, G. (1979). The NEL oscillating water column: recent developments. In *First symposium on wave energy utilization*.

[7] Newman, J. (1979). Absorption of wave energy by elongated bodies. *Applied Ocean Research*, 1(4):189–196.

[8] Newman, J. (1997). Wave effects on hinged bodies. Part I - body motions. Technical report. Accessed: June 2017.

[9] Newman, J. (2001). Wave effects on multiple bodies. *Hydrodynamics in ship and ocean engineering*, 3:3–26.

[10] Noad, I. and Porter, R. (2017). Approximations to wave energy absorption by articulated rafts. *Submitted to SIAM J. Appl. Math.*

[11] Noad, I. F. and Porter, R. (2015). Optimisation of arrays of flap-type oscillating wave surge converters. *App Ocean Res*, 50:237–253.

[12] Parisella, G. and Gourlay, T. (2016). Comparison of open-source code NEMOH with WAMIT for cargo ship motions in shallow water. Accessed: June 2017.

[13] Porter, R. (2016). Surface wave interaction with rigid plates lying on water. *Wave Motion*, 66:118–131.

[14] Rusu, L. and Onea, F. (2017). The performance of some state-of-the-art wave energy converters in locations with the worldwide highest wave power. *Renewable and Sustainable Energy Reviews*, 75:1348–1362.

[15] Salter, S., Jeffery, D., and Taylor, J. (1976). The architecture of nodding duck wave power generators. *The Naval Architect*, 1:21–24.

[16] Stansell, P. and Pizer, D. J. (2013). Maximum wave-power absorption by attenuating line absorbers under volume constraints. *Applied Ocean Research*, 40:83–93.

[17] Thomas, G. (2008). The theory behind the conversion of ocean wave energy: A review. In *Ocean Wave Energy*, pages 41–91. Springer.

[18] WAMIT (2017). `http://www.wamit.com/`. Accessed: June 2017.

[19] Yemm, R., Henderson, R., and Taylor, C. (2000). The OPD Pelamis WEC: Current status and onward programme. In *Proc. 4th European Wave Energy Conference, Aalborg Denmark*.